Figures-of-Merit for Rolling-Friction-Based Triboelectric Nanogenerators

Tao Jiang, Wei Tang, Xiangyu Chen, Chang Bao Han, Long Lin, Yunlong Zi, and Zhong Lin Wang*

Triboelectric nanogenerators (TENGs) have emerged as a highly effective and easily scalable technology for harvesting mechanical energy. Recently, standards and figure-of-merits have been defined to quantify the performance of TENGs. In this work, the figure-of-merits of rolling-friction-based TENGs are investigated through a theoretical model based on the rolling freestanding mode, including the conductor-to-dielectric and dielectric-to-dielectric cases. By combining finite-element simulations and semi-analytical derivations, the basic properties and resistive load output characteristics of rolling TENGs are calculated for various structural parameters, such as the electrode gap or rod diameter. The average output power is optimized by maximizing the structural figure-of-merit, which depends on the structural parameters. The results gained in this work could provide useful guidance for optimizing the performance of rolling-friction-based TENGs toward practical self-powered systems.

1. Introduction

Being able to scavenge energy from the ambient environment has attracted considerable interest due to the increasing consumption of fossil fuels and related environmental issues.[1–5] Mechanical energy, as a universally available and sustainable resource, is present on extensive energy levels from human body movements to automobiles and even ocean waves. It has been harvested by approaches based on piezoelectrics,[6,7] electromagnetics,[8,9] electrostatics,[10] and so on. Recently, a new mechanical energy harvesting approach, in the form of triboelectric nanogenerators (TENGs), has been invented, which couples triboelectrification with electrostatic induction.[11–14] This technology exhibits distinct advantages in comparison to other harvesting approaches, such as its high power density, high efficiency, low fabrication cost, and no pollution. In TENGs based on one of the four basic working modes, namely, contact mode, sliding mode, single-electrode mode,

and freestanding mode,[15–18] the energy conversion efficiency and device durability may be limited by the frictional resistive force between triboelectric surfaces, especially for the sliding-friction-based TENG.[19–21] Compared to in-plane sliding friction, rolling friction not only consumes less mechanical energy but also results in a higher robustness with minimized wearing of the materials.[21,22] In a previous work, a rolling triboelectric nanogenerator (RTENG) based on the rolling electrification between cylindrical steel rods and planar thin films of fluorinated ethylene propylene (FEP) was reported, and a high energy conversion efficiency of 55% was demonstrated, with a smaller surface wearing due to the low friction coefficient of the rolling movement.[21] Despite the unique merit of RTENGs, so far a systematic theoretical model to provide an in-depth understanding of their working principle is still lacking, and the issue of how to optimize their output performance remains to be studied.

Recently, a standard method to quantitatively evaluate the performance of TENGs was proposed by Wang's group.[23] The performance figure-of-merit for TENGs was defined, consisting of a structural figure-of-merit (FOM$_S$), related to the structural design, and a material figure-of-merit (FOM$_M$), related to the square of the surface charge density. Hence, the performance FOM is directly proportional to the highest possible average output power and associated with the highest achievable energy conversion efficiency, regardless of the mode and size of the TENG. Standards and evaluation methods would facilitate the comparison of various TENGs and lay the foundation for further applications of TENG technology. In the above-mentioned report, the structural FOM for various working modes was calculated using analytical formulae and finite-element simulations and it was found that the freestanding configuration possesses the highest FOM$_S$ because of the lower capacitance between the electrodes. Besides the effect of the working mode, it should be possible for a certain working mode to explore the impact of structural design on the structural FOM, which was not included in the previous work, such as the electrode-gap effect for freestanding TENGs.

In the present work, a theoretical model of rolling-friction-based TENGs in a rolling, freestanding mode was constructed. The finite-element method (FEM) and theoretical equations were applied to reveal the fundamental physics and dynamic output characteristics of rolling TENGs for both

Dr. T. Jiang, Prof. W. Tang, Prof. X. Chen,
Prof. C. B. Han, Prof. Z. L. Wang
Beijing Institute of Nanoenergy and Nanosystems
Chinese Academy of Sciences;
National Center for Nanoscience
and Technology (NCNST)
Beijing 100083, P. R. China
E-mail: zlwang@gatech.edu
Dr. L. Lin, Dr. Y. L. Zi, Prof. Z. L. Wang
School of Materials Science and Engineering
Georgia Institute of Technology
Atlanta, GA 30332-0245, USA

conductor-to-dielectric and dielectric-to-dielectric types. The influence of the structural parameters, including the electrode gap and rod diameter, on the basic properties and average output power were mainly addressed. Furthermore, the structural figure-of-merit was numerically calculated for various structural parameters, providing strategies for performance optimization of rolling TENGs.

2. Conductor-to-Dielectric Rolling-Friction-Based TENGs

A rolling-friction-based TENG in the freestanding mode has two categories: conductor-to-dielectric and dielectric-to-dielectric, according to the materials of the freestanding rolling rods. The FEM model for the conductor-to-dielectric rolling TENG (metal RTENG) was built with dimensions close to those of the real device, as shown in **Figure 1**a. Considering that the width w of the whole structure (10 cm) is much larger than the film thickness (0.1 mm), a 2D model was utilized to simplify the calculations. Two metal electrodes (Metal 1 and Metal 2, with a thickness of 0.01 mm each and length l = 10 cm) with a gap g (2 cm) in between them are coated with a dielectric layer that covers the electrodes and the gap (dielectric: ε_r = 2, a thickness of 0.1 mm, represented by d). The diameter of the metal rods is defined as d_r, and the rods are arranged closely in line with a total length of l. The rods are rolling from the left of the dielectric (the rolling displacement is represented by x). For clarity, a

top-view diagram of the TENG structure is plotted in Figure S1 in the Supporting Information. The charge density at the upper surface of the dielectric was assigned as $-\sigma$ (10 µC m^{-2}). Because of charge conservation, the rolling rods have the same amount of charge as the dielectric surface. The length and width of the upper surface of the dielectric are $2l + g$ and w, respectively, so the rods have positive charges with a total amount of $\sigma w(2l + g)$.

The FEM calculations under short-circuit (SC) and open-circuit (OC) conditions were carried out using COMSOL software. The metal rods were assigned with the same electric potential to reflect the direct contact. The initial state where the left sides of the rods and the dielectrics overlap under the SC condition was chosen as the charge reference state, and the SC charge Q_{SC} was calculated as the total transferred charges under SC ($Q_{net,SC}$) subtracted by the charges at such reference state, similar to previously reported work.[24,25] The total capacitance C, which is an inherent character of the TENG that is independent of the reference state, was extracted by the linear interpolation from the FEM results based on the V-Q-x relationship.[26,27] Then the OC voltage V_{OC} was obtained from the relation $V_{OC} = Q_{SC}/C$.

The typical OC electric potential distributions for various rolling displacements x under the charge reference state are shown in Figure 1b. The electrode gap was fixed as g = 2 cm, and the rod diameter d_r was set to be 2 mm. As x increased from zero to maximum displacement ($l + g$ = 12 cm), the potential difference between Metal 2 and Metal 1 first increased
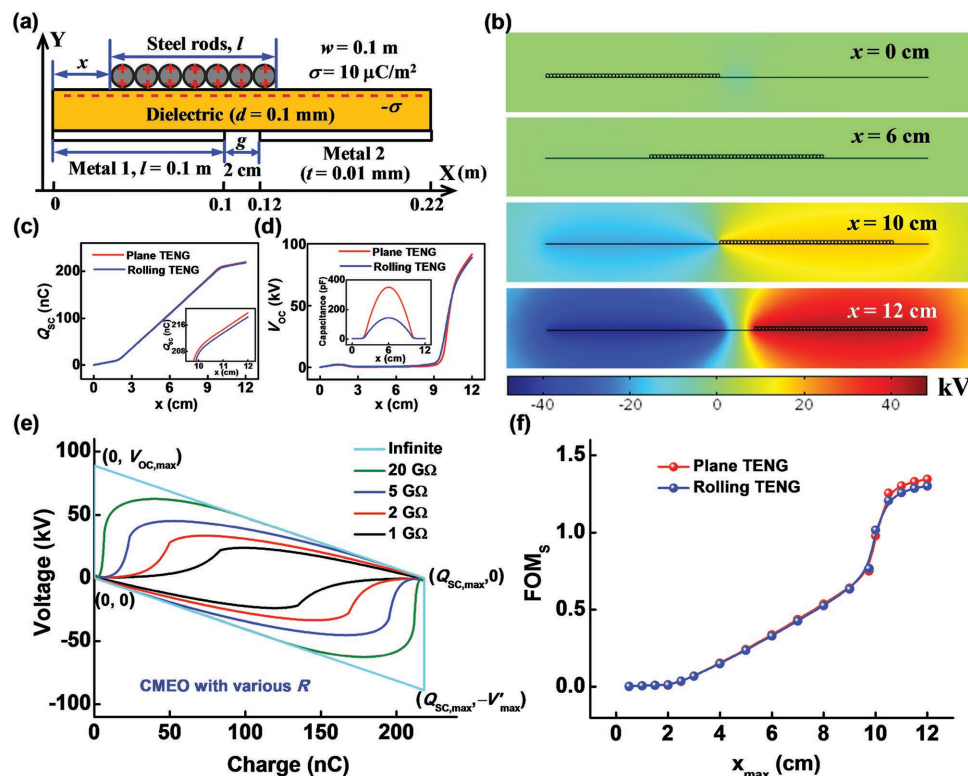
Figure 1. a) FEM model of a rolling-friction-based TENG. b) Electric potential distribution for various rolling displacements under the charge reference state. c,d) Short-circuit charge, Q_{SC}, open-circuit voltage, V_{OC}, and capacitance, C, as a function of x for plane and rolling TENGs. e) CMEO for various load resistances for a rolling TENG with x_{max} = 12 cm. f) Structural figure-of-merit, FOM$_S$, versus x_{max} for two TENGs.

www.MaterialsViews.com

ADVANCED
MATERIALS
TECHNOLOGIES
www.advmattechnol.de

FULL PAPER

slowly and then increased sharply up to around 90 kV, and the open-circuit voltage V_{OC} followed the same trend (Figure 1d). The sharp increase in the V_{OC} can be ascribed to the quick drop in capacitance (inset of Figure 1d). The Q_{SC} curve indicates that the Q_{SC} slightly increases in the displacement range of $0 \leq x \leq g$ and $l \leq x \leq l + g$, but follows a rapid linear increase in the middle range (Figure 1c). A comparison between a plane TENG and a rolling TENG is made in Figure 1c,d, where the freestanding layer of the plane TENG is a metal layer with a length of 10 cm and a thickness of 0.01 mm. It can be seen that the two Q_{SC} curves nearly overlap, and the maximum Q_{SC} and V_{OC} of the rolling TENG are slightly smaller than those of the plane TENG (inset in Figure 1c). The capacitance of the rolling TENG exhibited an obvious decrease due to the raised mass center of the freestanding layer.

Similar to a previous report in the literature,[23] to capture the cycles for maximized energy output (CMEO) of the TENG, a switch in parallel with a load resistor was turned off and on alternately. The following repeated steps were performed: rolling of metal rods from $x = 0$ to $x = l + g$ at switch off; turn the switch on to realize the maximum transferred charge; rolling of metal rods back from $x = l + g$ to $x = 0$ at switch off; turn the switch on to enable zero charge. The CMEO at the resistance R result in voltage–charge (V–Q) curves, which can be obtained by the interpolation method and semi-analytical solution of the V-Q-x relationship.[28–30] Coupling this with Ohm's law, the governing equation of the RTENG is given by

$$R \frac{dQ}{dt} = V = -\frac{1}{C(x)} \times Q + V_{OC}(x) \tag{1}$$

where $1/C(x)$ and $V_{OC}(x)$ are obtained by the continuous fraction interpolation based on the FEM results. By specifying the motion process, for example, a harmonic motion, in which $x(t)$ is defined as

$$x(t) = \frac{x_{max}}{2} \left(1 - \cos\left(\frac{\pi v t}{x_{max}}\right) \right) \tag{2}$$

where x_{max} is the maximum rolling displacement, and v is 1.0 m s^{-1}, the differential equation can be solved, and the Q-t, V-t equations at the first half cycle with the boundary condition of $Q(t = 0) = 0$ are given as

$$Q = \frac{1}{R} \exp\left(-\int_0^t \frac{dt}{RC(x(t))}\right) \int_0^t V_{OC}(x(t)) \exp\left(\int_0^t \frac{dz}{RC(x(z))}\right) dt \tag{3}$$

$$V = V_{OC}(x(t)) - \frac{1}{RC(x(t))} \exp\left(-\int_0^t \frac{dt}{RC(x(t))} \int_0^t V_{OC}(x(t))\right)$$

$$\exp\left(\int_0^t \frac{dz}{RC(x(z))}\right) dt \tag{4}$$

At the second half cycle, the differential equation is similarly solved under the boundary condition of $Q(t = x_{max}/v) = Q_{SC,max}$ ($Q_{SC,max}$ is the maximum SC transferred charge).

The CMEO for various load resistances for the metal RTENG with $x_{max} = 12$ cm are plotted in Figure 1e. As can be seen, the output energy per cycle of the CMEO is higher for larger external load resistances, R, as observed from the V–Q curves. When the R is infinitely large, the maximized output energy per cycle can be achieved. In this case, we removed the load resistor to continue the simulations, therefore, the "switch-off" state becomes the OC state, and the "switch-on" state is the SC state. The CMEO at such state exhibits a rhomboidal shape, whose vertices are determined by the maximum OC voltage, $V_{OC,max}$, maximum SC charge, $Q_{SC,max}$, and the maximum achievable absolute voltage V'_{max} at $Q = Q_{SC,max}$. It can be found that the V'_{max} is equivalent to $V_{OC,max}$ at $x_{max} = 12$ cm due to the structural symmetry (the capacitances at $x = 0$ and $x = l + g$ are the same). If the x_{max} is smaller than 12 cm, the V'_{max} is not equal to $V_{OC,max}$ (the CMEO has a trapezoidal shape), because the $V_{OC,max}$ is given by $Q_{SC,max}/C(x_{max})$, whereas the V'_{max} is obtained by $Q_{SC,max}/C(0)$. Through calculating the largest possible output energy per cycle, E_m, the performance FOM (FOM$_P$) of the TENG can be further calculated as[23]

$$FOM_P = FOM_S \cdot \sigma^2 = 2\varepsilon_0 \frac{E_m}{A x_{max}} \tag{5}$$

where ε_0 is the vacuum permittivity, A is the tribo-surface area of the dielectric layer, and FOM$_S$ and E_m are given by

$$FOM_S = \frac{2\varepsilon_0}{\sigma^2} \frac{E_m}{A x_{max}}, \quad E_m = \frac{Q_{SC,max}}{2} (V_{OC,max} + V'_{max})$$

In the calculations, the charge density σ was kept constant (FOM$_M$ was unchanged), and the dimensionless FOM$_S$ was mainly considered. The structural figure-of-merits (FOM$_S$) as a function of x_{max} were calculated for a plane and rolling TENG and are shown in Figure 1f. As the x_{max} increased, the FOM$_S$ curve shows three regions: first, a constant region ($0 \leq x \leq g$), in the middle a linearly increasing region ($g \leq x \leq l$), and, finally, a sharply increasing region ($l \leq x \leq l + g$). It reaches a maximum value at $x_{max} = l + g$ for both the plane and rolling TENGs, and the maximum FOM$_S$ of the rolling TENG is slightly lower than that of the plane TENG.

To get an in-depth understanding of the output performance for the metal RTENG, we calculated the real-time dynamic resistive load characteristics during the harmonic motion as shown in Equation (2). By applying the periodic boundary conditions[29,31]

$$Q(t = 0) = Q\left(t = \frac{2x_{max}}{v}\right) \tag{6}$$

the steady-state transferred charge Q of the RTENG for an arbitrary load resistance R is obtained:

$$Q = \exp\left(-\int_0^t \frac{dt}{RC(x(t))}\right)$$

$$\times \left[Q_0 + \int_0^t \frac{V_{OC}(x(t))}{R} \exp\left(\int_0^t \frac{dz}{RC(x(z))}\right) dt \right], 0 \leq t \leq \frac{x_{max}}{v} \tag{7a}$$

**ADVANCED
MATERIALS
TECHNOLOGIES**

www.advmattechnol.de

*Materials
Views*

www.MaterialsViews.com

FULL PAPER

$$Q = \exp\left(-\int_{\frac{x_{max}}{v}}^{t} \frac{dt}{RC(x(t))}\right)$$
$$\times \left[Q\left(\frac{x_{max}}{v}\right) + \int_{\frac{x_{max}}{v}}^{t} \frac{V_{OC}(x(t))}{R} \exp\left(\int_{\frac{x_{max}}{v}}^{t} \frac{dz}{RC(x(z))}\right) dt\right], \quad (7b)$$
$$\frac{x_{max}}{v} \leq t \leq \frac{2x_{max}}{v}$$

where Q_0 is given by

$$Q_0 = \frac{\exp\left(-\frac{2}{R}\int_0^{\frac{x_{max}}{v}} \frac{dt}{C(x(t))}\right) \times \int_0^{\frac{x_{max}}{v}} \frac{V_{OC}(x(t))}{R} \exp\left(\int_0^{t} \frac{dz}{RC(x(z))}\right) dt}{+\int_0^{\frac{x_{max}}{v}} \frac{V_{OC}(x(t))}{R} \exp\left(-\int_0^{t} \frac{dz}{RC(x(z))}\right) dt}{1 - \exp\left(-\frac{2}{R}\int_0^{\frac{x_{max}}{v}} \frac{dt}{C(x(t))}\right)}$$

Through the differentiation of Q by t, we can obtain the equations of the steady-state current I for the arbitrary load resistance and then the steady-state voltage V can be calculated using Ohm's law. After that, the average output power P_{ave} can be calculated according to:

$$P_{ave} = \frac{\int_0^T I^2 R \, dt}{T}, \quad T = \frac{2x_{max}}{v} \quad (8)$$

The numerical calculation results of the steady-state Q, I, V at various load resistances for a metal RTENG with $g = 2$ cm are presented in **Figure 2**a–c. Periodic waves with a period of
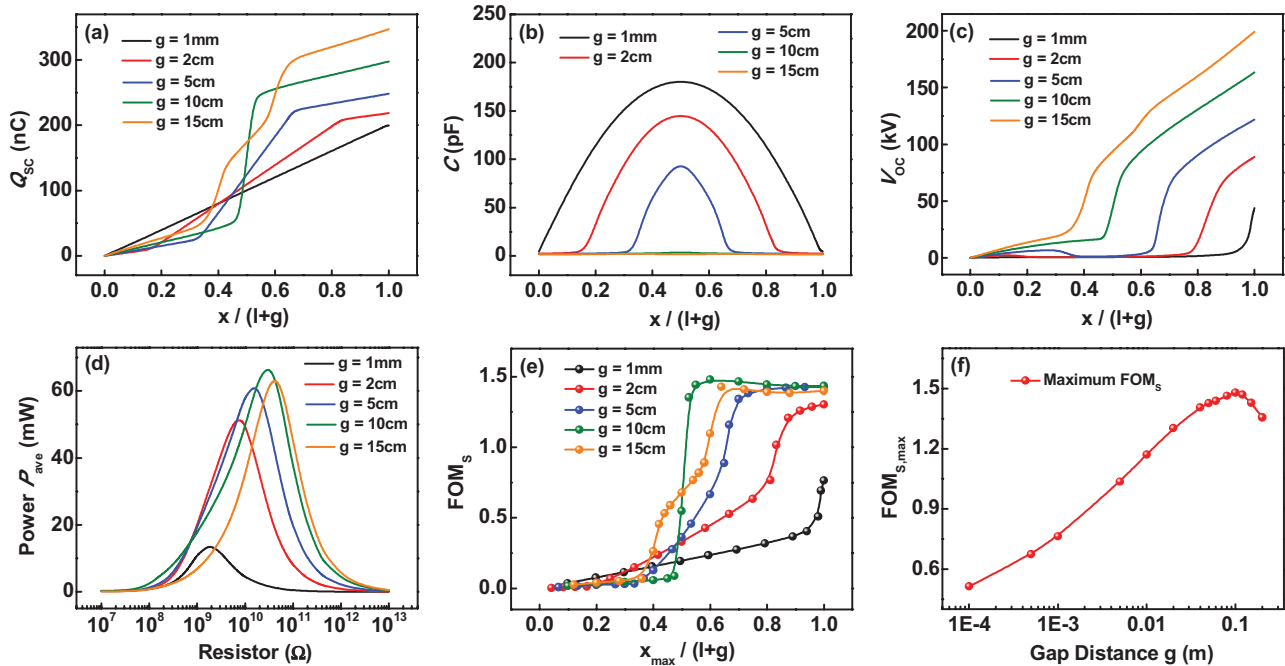
$2x_{max}/v$ (0.24 s) were obtained for all Q-t, I-t, and V-t curves. Under short-circuit conditions these curves were symmetrical with respect to the half cycle. As the resistance R increased, the curves deviated gradually from the SC state, and the oscillation magnitude of the Q curve decreased gradually due to the increasing limitations of charge transport. The charge at infinitely large resistance remained constant at half of the maximum Q_{SC}. The peak of the current curve first increased from the SC current and then decreased until 0 at the OC state. The peak of the voltage curve also increased first and then slightly decreased to its saturation value. The V peak at 10 GΩ can exceed the V peak at infinitely large resistance, because the voltage curve at infinitely large resistance obtained using the periodic boundary conditions is not the same as the V_{OC}.[31] The metal RTENG shows a three-working-region behavior, which is inherent because of the "impedance" match of the TENG capacitance and the load resistance. When R matches the impedance of the TENG, a maximum average output power, P_{ave}, can be reached at an optimum resistance of about 7 GΩ (Figure 2d).

The gap distance between the two electrodes (g) is an important design parameter that can greatly affect the output characteristics of a freestanding TENG because of its impact on the capacitance between electrodes.[24,25] The influence of g on the total output performance for a metal RTENG with $x_{max} = 12$ cm and $d_r = 2$ mm was examined and plotted as shown in **Figure 3**. When the gap g was varied, the electrode length l was fixed, but the length of the dielectric was correspondingly changed, leading to a change in the amount of tribo-charge. The Q_{SC}, C, and V_{OC} as a function of $x/(l + g)$ for a metal RTENG with
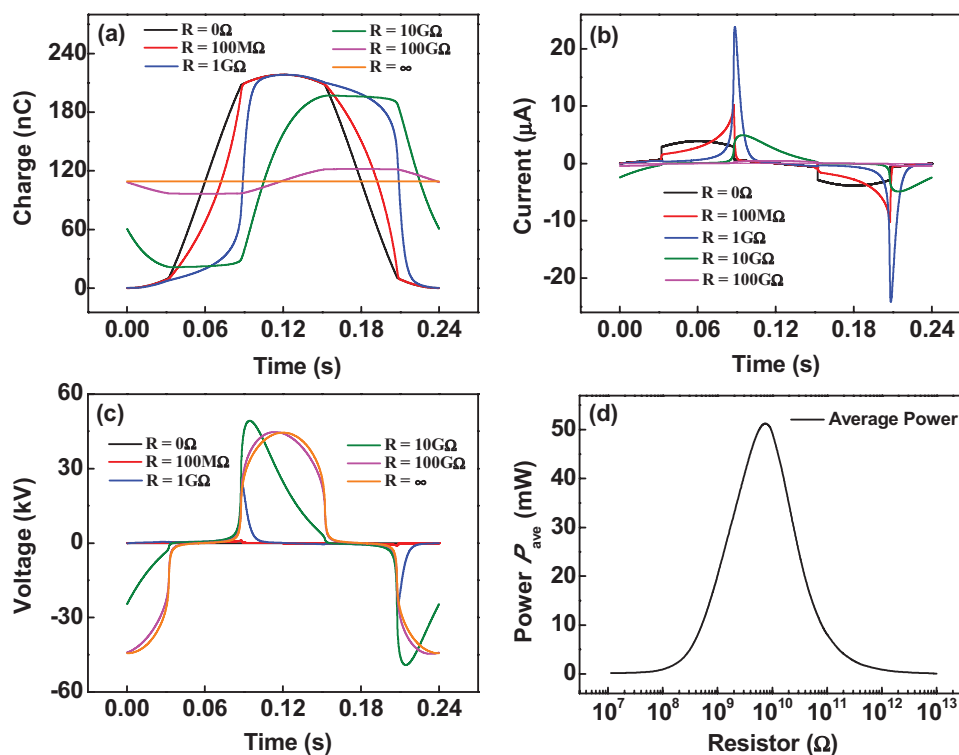
Figure 2. a–c) Charge-time, current-time, and voltage-time relationships at various resistances for a metal RTENG with $g = 2$ cm. d) Average power with respect to the resistance R for this TENG.

www.MaterialsViews.com

ADVANCED
MATERIALS
TECHNOLOGIES
www.advmattechnol.de

FULL PAPER

Figure 3. a–c) Short-circuit charge, Q_{SC}, capacitance, C, and open-circuit voltage, V_{OC}, as a function of $x/(l + g)$ for metal RTENGs with various g. d) Average power versus R for various g. e) FOM$_S$ versus $x_{max}/(l + g)$ for various g. f) Maximum FOM$_S$ for various g.

various g are shown in Figure 3a–c. For a very small rod diameter (2 mm), the charge transfer efficiency can reach 100%, and the maximum value of Q_{SC} is then equal to the amount of tribo-charge. It can be seen that the Q_{SC} follows the same trend for all g values, in other words, a slow increase is seen at the two ends and a sharp increase is seen in the middle, and the maximum Q_{SC} increases with g because of the increase in tribo-charge. Note that for $g > l$, a folding distortion appears in the middle region of the Q_{SC} curve, which may be ascribed to the edge effect. The total capacitance of the metal RTENG decreased with increasing g, but this decrease is the result of two parts. First, the direct parasitic capacitance between the two electrodes decreases with g. Second, the overlapping region between the metal rods and both electrodes decreases with increasing g, leading to a decrease in the serial connection of capacitances between the top metal and Metal 1 and between the top metal and Metal 2. When g is larger than l, the freestanding rods cannot overlap with both electrodes, and only a parasitic capacitance exists. The V_{OC} can attain its maximum value for all g values when full separation is reached, and the maximum V_{OC} increases with increasing g (Figure 3c). It should be noted that for smaller g values, the V_{OC} curve has a small peak at smaller x because of the competition of the increasing speed of Q_{SC} and C, and for larger g, the V_{OC} curve is higher at smaller x. Because of the nonlinear distortion, the V_{OC}-x equation should be captured by a step-wise interpolation method.

The average output power dependent on R during the harmonic mechanical motion with a period of T was calculated for various g values. The result in Figure 3d indicates that there is an optimum gap for the metal RTENG to generate the highest average power, and the optimum resistance (the resistance at which P_{ave} is maximized) shifts significantly to higher

values with increasing g because of the according decrease in capacitance. When g first increased from 0, the period length T increased only a little because l still dominated the total period length, and the maximum V_{OC} dominated the increase in P_{ave}. However, when g became large enough, the decreasing slope of the total capacitance became flattened, and the increase in maximum V_{OC} could not catch up with the increasing speed in T, leading to a drop in P_{ave}.

From the above-mentioned, we found that the average output power in the specific motion mode (harmonic motion) can be controlled by adjusting the electrode gap. As a matter of fact, the potential output performance, that is, the greatest possible average output power, which is reflected by the structural FOM, may be different for different structural parameters (e.g., electrode gap). The FOM$_S$ with respect to the $x_{max}/(l+g)$ was simulated for various g, as shown in Figure 3e. At smaller g, the FOM$_S$ first remained steady followed by a linear increase, similar to the shape of the Q_{SC} curve, and then sharply increased, like the V_{OC} curve. This implies that the FOM$_S$ is determined by the competition between Q_{SC} and V_{OC} for smaller gaps. The maximum FOM$_S$ (FOM$_{S,max}$) can be reached at the maximum rolling displacement ($x_{max} = 12$ cm). When g was increased up to 5 cm, the FOM$_S$ exhibited two flat regions at either end and one sharp region in the middle, similar to the shape of the Q_{SC} curve, indicating that the Q_{SC} dominates the FOM$_S$ as a function of x_{max} for larger gaps. At the end of the FOM$_S$-x_{max} curve, a slight decrease in the FOM$_S$ makes the FOM$_{S,max}$ appear at a slightly lower x_{max} than the maximum x_{max}. The FOM$_{S,max}$ was extracted for various g values and there is an optimum gap in order to obtain the maximum value (Figure 3f). The optimization of the structural FOM will provide an effective route toward optimizing the potential output performance of metal RTENGs.

Apart from the electrode gap, the diameter d_r of the top metal rods is another important structural parameter that has a direct impact on the output properties of the TENG. The total length of the metal rods in the horizontal direction was kept constant (l), therefore a change in d_r represents a change in the number of cylindrical rods. The results of Q_{SC}, C, and V_{OC} for a metal RTENG with various d_r values at a fixed g (2 cm) are presented in **Figure 4**a,b. As the d_r increased from 2 mm to 1 cm, the Q_{SC} remained nearly unchanged; however, for $d_r = 2$ cm, the Q_{SC} showed small, nonlinear distortions near the $x = g$ and $x = l$ regions. When d_r was increased up to 5 cm, the Q_{SC} exhibited a ladder-like character due to the flattened capacitance for the middle x range (inset of Figure 4a). The d_r did not significantly influence the maximum Q_{SC}, and the charge-transfer efficiency can reach nearly 100% for any d_r value. The capacitance C at the middle position was found to decrease markedly with increasing d_r. This is because the mass centers of the metal rods are higher at a larger d_r, which induces a decrease in the serial capacitance between the top metal and the two electrodes. Figure 4b shows that the V_{OC} increased at smaller x with increasing d_r due to the decreasing capacitance, whereas it decreased at larger x. The maximum V_{OC} decreased with increasing d_r, because of a slight increase in capacitance at full separation, where the total capacitance resulted mainly from the parasitic capacitance between the two electrodes.

Subsequently, the average output power for the metal RTENG with various d_r was numerically calculated, as shown in Figure 4c. The peak value of P_{ave} (optimum power) decreased with increasing d_r, where the generated power was mainly determined by V_{OC}. Th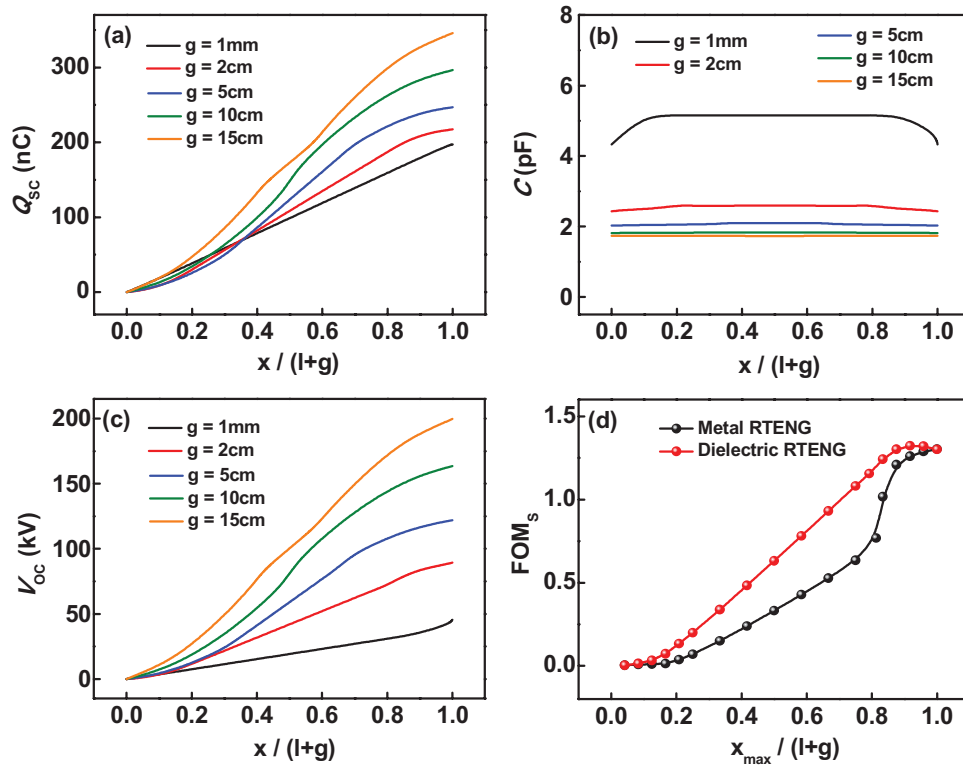e optimum resistance shifted slightly toward larger values, which may be ascribed to the decrease in average capacitance. The impedance of the inherent capacitance of a TENG can be expressed as $1/\omega C$, but C is the average capacitance, because the capacitance is time-dependent due to the changes in the position of the metal rods.

In addition, the FOM_S with respect to the $x_{max}/(l + g)$ was studied and plotted, indicating that the maximum FOM_S also decreased when the rods became thicker (Figure 4d). For d_r varying from 2 mm to 2 cm, we first observed a constant region, then a middle, linearly increasing, region, and finally a sharply increasing region was observed, due to the combined action of Q_{SC} and V_{OC}. For a d_r of 5 cm, the sharp region for the FOM_S was seen at a smaller x_{max}, and there was a drop at the end, which may result from the staged Q_{SC}. The above results for the FOM_S reveal that metal RTENGs possess higher potential output performances if thinner metal rods are used. The most extreme case is a plane TENG, which has a slightly higher FOM_S than the rolling TENG, as shown in Figure 1f. However, considering its better material-wearing and device-durability properties, the rolling TENG is the desirable choice as only a slight decrease in the structural FOM was found.

The theoretical predictions on the structural dependence of the output performance for metal RTENGs were compared with our previous experimental results. In this previous work, for a RTENG device containing cylindrical steel rods and a planar FEP film, increasing the gap distance between the two electrodes on each FEP film resulted in slight enhancement in the V_{OC}, whereas the current density, J_{SC}, decayed drastically. The optimum output power density also decreased with increasing gap distance. However, in the present work, an optimum gap
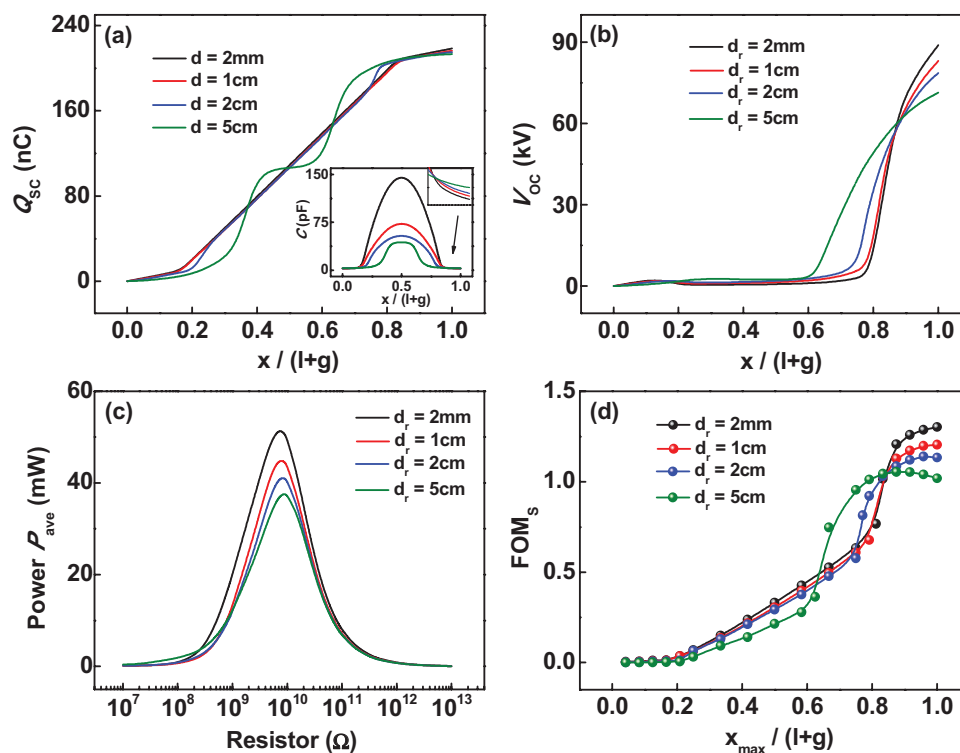
Figure 4. a,b) Q_{SC}, C, and V_{OC} as a function of $x/(l + g)$ for metal RTENGs with various rod diameters, d_r, at $g = 2$ cm. c) Average power versus R for various d_r. d) FOM_S versus $x_{max}/(l + g)$ for various d_r.

Materials
Views
www.MaterialsViews.com

ADVANCED
MATERIALS
TECHNOLOGIES
www.advmattechnol.de

FULL PAPER

Figure 5. a–c) Short-circuit charge, Q_{SC}, capacitance, C, and open-circuit voltage, V_{OC}, as a function of $x/(l + g)$ for dielectric RTENGs with various g. d) Comparison of FOM$_S$ with respect to $x_{max}/(l + g)$ for a metal RTENG and a dielectric RTENG with $g = 2$ cm.

distance was observed that led to a maximum average power. The difference is that in the experimental device the electrode lengths were adjusted rather than the FEP film length when varying the electrode gap. The constant charge amount and longer charge-transfer time thus led to decreases in the current and power. On the other hand, the dependence of the output power on the rod diameter of the experimental set-up was in good agreement with our theoretical results. The V_{OC}, J_{SC}, and power density all decreased with an increase in the diameter of the rolling rods, because the distance between the charge center and the electrodes steadily increased.

3. Dielectric-to-Dielectric Rolling-Friction-Based TENG

Apart from the conductor-to-dielectric RTENG, the output characteristics and figure-of-merit of the dielectric-to-dielectric type of RTENG (dielectric RTENG) were also investigated. In the FEM model of a dielectric RTENG, the freestanding metal rods were replaced with dielectric rods. The relative permittivity of these dielectric rods with diameter d_r was chosen to be $\varepsilon_{r2} = 5$. The contact electrification between the dielectric rods and the dielectric layer on top of the electrodes generated net positive electrostatic charges on the surface of the dielectric rods and net negative charges on the surface of the dielectric layer. Under SC and OC conditions, the charge density on the upper face of the dielectric layer was assigned as $-\sigma$, and the rod surfaces attained a charge density of $(2l + g)\sigma/\pi l$ due to charge

conservation. For the dielectric layer and the dielectric rods, the charge density of the uniformly distributed charges was assigned to be on the surface. The charge density at the surface of the dielectric rods was calculated based on the total lateral area of the rods. In contrast, for the metal rods, the total charge amount was assigned to be equal to the charge amount on the dielectric surface, because the charges in the metal rods could move freely. This forms a criterion for assigning the triboelectric charge of TENGs with different materials. The charge density at the surface of the planar dielectric layer was kept the same for both the conductor-to-dielectric and dielectric-to-dielectric types, because the dielectric layers contained the same material for both TENG types. The size parameters and other boundary conditions for the dielectric-to-dielectric RTENG were also the same as those of the metal RTENG.

The Q_{SC}, C, and V_{OC} for the dielectric RTENG with $d_r = 2$ mm as a function of the gap g were simulated and are shown in **Figure 5**a–c. As g increased, the maximum Q_{SC} and V_{OC} both increased, whereas the C decreased, as was the case for the metal RTENG. The charge-transfer efficiency attained was still 100% for all g values, and the maximum Q_{SC} equalled the amount of tribo-charges. The increase in the tribo-surface area and charges with g led to an increase in the maximum Q_{SC}. The capacitance profiles were nearly constant, because the total capacitance resulted mainly from the parasitic capacitance between the two electrodes, without any metal screening effect. Therefore, the V_{OC} curves had the same shape as the Q_{SC} curve (a gradual increase with respect to x). The difference between the Q_{SC}, C, and V_{OC} of the dielectric RTENG and those of the
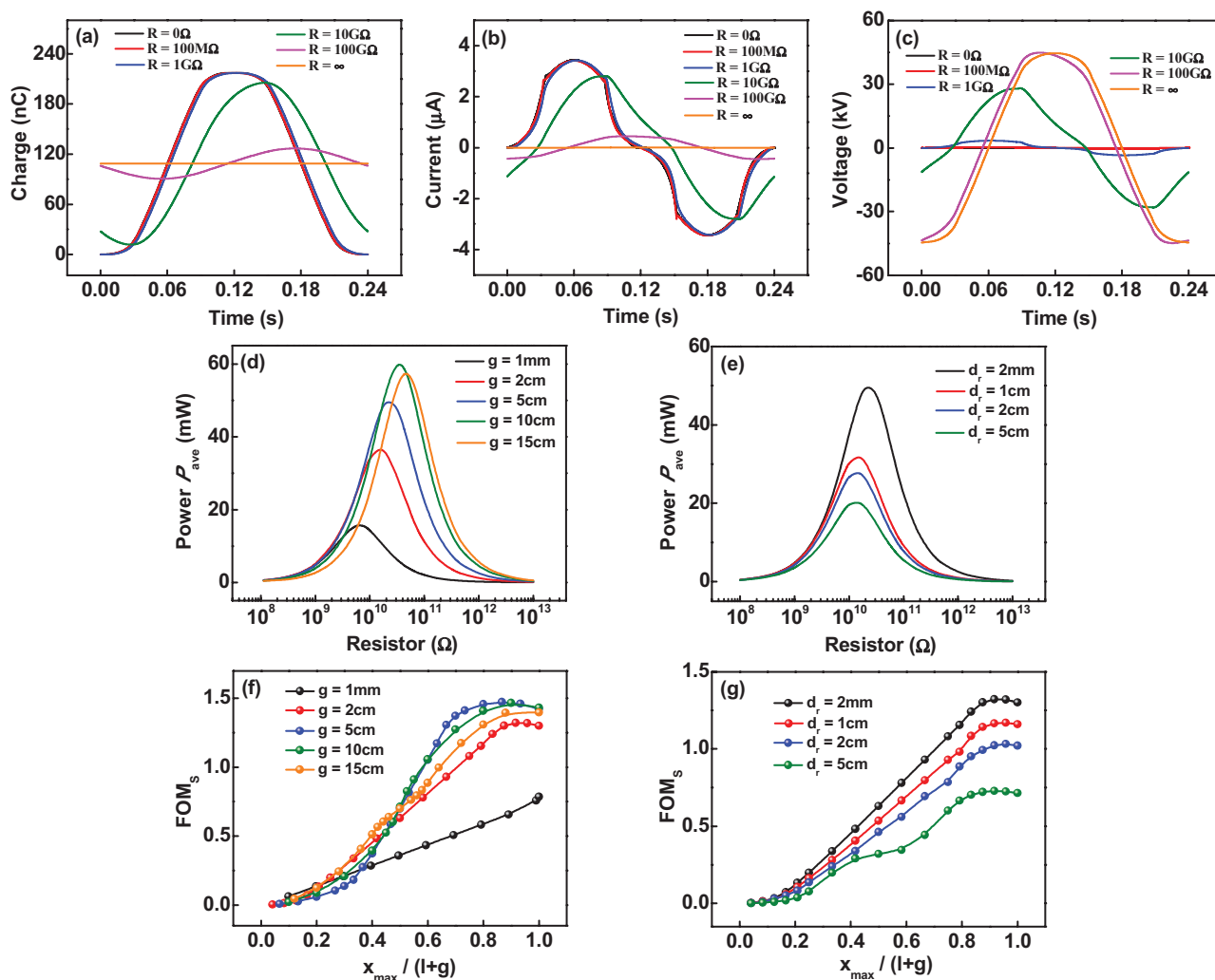
Figure 6. a–c) Charge-time, current-time, and voltage-time relationships at various resistances for a dielectric RTENG with $g = 2$ cm. d,e) Average power versus R for various g and d_r. f,g) FOM$_S$ versus $x_{max}/(l + g)$ for various g and d_r.

metal RTENG can be found by comparing the results shown in Figure S2a-c in the Supporting Information. The structural FOM of the dielectric RTENG was also calculated and compared with that of the metal RTENG (Figure 5d, $g = 2$ cm). Different from that of the metal RTENG, the FOM$_S$ curve of the dielectric RTENG had two flat regions at either end and one middle region that showed a linear increase, which was similar to the results found for the Q_{SC} and V_{OC} curves. The FOM$_S$ of the dielectric RTENG was higher than that of the metal RTENG due to the higher V_{OC}, although the FOM$_S$ values for both RTENGs at $x_{max} = l + g$ were the same.

The resistive load output characteristics were also studied for the dielectric RTENG. The real-time Q-t, I-t, and V-t relationships at various load resistances for $g = 2$ cm and $d_r = 2$ mm are shown in **Figure 6**a–c. During the harmonic motion process, the output curve was nearly harmonic, but not a pure harmonic curve, as it contained some nonlinear distortion because of the nonlinear V_{OC}-x characteristics. The V_{OC}-x curve was only nonlinear at the two ends, and the capacitance was quite close to being constant (see Figure 5), therefore, the nonlinear

distortion was not severe in the Q-t, I-t, and V-t curves. When R was increased from 0 to 100 MΩ, the impedance of the TENG capacitance ($1/\omega C$) was much larger than R, and the Q and I profiles remained close to the SC profile. With increasing R, the total impedance of the serial connection of $1/\omega C$ and R slowly increased too, leading to a decrease of the current amplitude and an increase in the voltage amplitude. Compared to the metal RTENG, in the dielectric RTENG the current amplitude for any resistance cannot exceed the SC current amplitude, and the voltage attains the maximum amplitude under OC conditions. The dielectric RTENG delivered a lower optimum power at a higher optimum resistance, which is dependent of the capacitance (Figure S2d, Supporting Information).

The influences of the structural parameters, namely, the electrode gap and the rod diameter, on the average power P_{ave} and structural FOM for the dielectric RTENG are revealed in Figure 6d–f. When studying the effect of g, the d_r was set to 2 mm, and when changing the d_r, the g was fixed at 2 cm. The trend of P_{ave} with g was found to be similar to that of the metal RTENG, in other words, the peak value of P_{ave} first

increased and then decreased with increasing g. The optimum power attained its maximum at an optimal gap because of the competition between the increasing speeds of V_{OC} and T, and the optimal resistance also increased with increasing g, as a result of the drop in capacitance. Moreover, the optimal power decreased with increasing d_r, and the optimal resistance decreased slightly. The effect of the rod diameter on the optimal resistance was different from that of the metal RTENG. That is because the capacitance is mainly related to the parasitic capacitance, which only slightly increased with d_r for the dielectric RTENG (Figure S3, Supporting Information). In addition, the Q_{SC} and V_{OC} with respect to x for various d_r were also different. The Q_{SC} and V_{OC} both gradually increased with increasing x, as opposed to the ladder-like increase of Q_{SC} and the sharp increase of V_{OC} (Figure S3a,c, Supporting Information) for the metal RTENG. The maximum Q_{SC} decreased with d_r, implying that an increase of d_r lowered the charge-transfer efficiency in the absence of the top-metal screening effect.

The above results provide the possibility to predict the output performance of a dielectric RTENG in the common harmonic motion process. For any motion mode, the possible highest performance was characterized by the structural FOM at a fixed material FOM, and the results of the FOM$_S$ are presented in Figure 6e,f. At a very small g (1 mm), the FOM$_S$ curve, as well as the Q_{SC} and V_{OC} curves, was approximately linear and the maximum FOM$_S$ was obtained at full separation ($x_{max} = 12$ cm). When g increased, the FOM$_S$ had two flat regions at either end and one middle region with a rapidly increasing curve because of the cooperative action between Q_{SC} and V_{OC}. At the end of the FOM$_S$-x_{max} curve, there was a slight decrease in the FOM$_S$. The FOM$_{S,max}$ was found to first rise and then subsequently drop as g increased. Therefore, an optimal gap could also be observed for the dielectric RTENG. On the other hand, the FOM$_{S,max}$ decreased markedly with increasing d_r. For $d_r = 5$ cm, the FOM$_S$ exhibited a staged character that resembled the shape of the Q_{SC} and V_{OC} curves, and the FOM$_{S,max}$ largely decreased to about 0.7. Through comparison, we found that the dielectric RTENG possessed a higher structural FOM at smaller electrode gap or rod diameter, whereas a lower structural FOM was found at larger electrode gap or rod diameter, which may serve as an important guideline for the rational structural design of RTENGs for specific applications.

4. Conclusions

We have constructed a theoretical model for rolling-friction-based TENGs for both the conductor-to-dielectric and dielectric-to-dielectric configurations. FEM simulations were performed to study the basic properties of RTENGs and the dynamic output characteristics at arbitrary load resistance were theoretically calculated. The results indicated that the Q_{SC}, C, and V_{OC} are influenced by the material of the freestanding rods, and by structural parameters, such as the electrode gap and rod diameter. We found that there is an optimal gap g for reaching a maximal average output power in a harmonic motion for both the metal and dielectric RTENGs, and the optimal power decreased with increasing diameter d_r. Also, the optimal resistance was greatly influenced by the structural parameters. More importantly, the structural FOM characterizing the greatest average output power possible was examined for both metal and dielectric RTENGs. The FOM$_S$ can be maximized by adjusting g and d_r, and the difference in the FOM$_S$ between the two RTENGs was demonstrated. The present work facilitates the comparison of RTENGs with different structural designs and deepens the understanding of potential performance improvements for RTENGs.

Supporting Information

Supporting Information is available from the Wiley Online Library or from the author.

[1] E. P. Murray, T. Tsai, S. A. Barnett, *Nature* **1999**, *400*, 649.
[2] A. Khaligh, O. C. Onar, *Energy Harvesting: Solar, Wind, and Ocean Energy Conversion Systems*, CRC Press, Boca Raton, FL **2009**.
[3] B. Z. Tian, X. L. Zheng, T. J. Kempa, Y. Fang, N. F. Yu, G. H. Yu, J. L. Huang, C. M. Lieber, *Nature* **2007**, *449*, 885.
[4] S. H. Wang, L. Lin, Z. L. Wang, *Nano Energy* **2015**, *11*, 436.
[5] Z. L. Wang, J. Chen, L. Lin, *Energy Environ. Sci.* **2015**, *8*, 2250.
[6] Z. L. Wang, J. H. Song, *Science* **2006**, *312*, 242.
[7] Y. Qin, X. D. Wang, Z. L. Wang, *Nature* **2008**, *451*, 809.
[8] C. B. Williams, C. Shearwood, M. A. Harradine, P. H. Mellor, T. S. Birch, R. B. Yates, *Proc. IEEE Circ. Dev. Syst.* **2001**, *148*, 337.
[9] S. P. Beeby, R. N. Torah, M. J. Tudor, P. Glynne-Jones, T. O'Donnell, C. R. Saha, S. Roy, *J. Micromech. Microeng.* **2007**, *17*, 1257.
[10] P. Basset, D. Galayko, A. M. Paracha, F. Marty, A. Dudka, T. Bourouina, *J. Micromech. Microeng.* **2009**, *19*, 115025.
[11] F. R. Fan, Z. Q. Tian, Z. L. Wang, *Nano Energy* **2012**, *1*, 328.
[12] W. Tang, T. Jiang, F. R. Fan, A. F. Yu, C. Zhang, X. Cao, Z. L. Wang, *Adv. Funct. Mater.* **2015**, *25*, 3718.
[13] C. B. Han, T. Jiang, C. Zhang, X. Li, C. Zhang, X. Cao, Z. L. Wang, *ACS Nano* **2015**, *9*, 12552.
[14] Y. N. Xie, S. H. Wang, S. M. Niu, L. Lin, Q. S. Jing, J. Yang, Z. Y. Wu, Z. L. Wang, *Adv. Mater.* **2014**, *26*, 6599.
[15] C. B. Han, W. M. Du, C. Zhang, W. Tang, L. M. Zhang, Z. L. Wang, *Nano Energy* **2014**, *6*, 59.
[16] X. Chen, M. Iwamoto, Z. Shi, L. Zhang, Z. L. Wang, *Adv. Funct. Mater.* **2015**, *25*, 739.
[17] Y. Yang, Y. S. Zhou, H. L. Zhang, Y. Liu, S. Lee, Z. L. Wang, *Adv. Mater.* **2013**, *25*, 6594.
[18] S. H. Wang, Y. N. Xie, S. M. Niu, L. Lin, Z. L. Wang, *Adv. Mater.* **2014**, *26*, 2818.
[19] G. Zhu, Y. S. Zhou, P. Bai, X. S. Meng, Q. S. Jing, J. Chen, Z. L. Wang, *Adv. Mater.* **2014**, *26*, 3788.
[20] G. Zhu, Y. J. Su, P. Bai, J. Chen, Q. S. Jing, W. Q. Yang, Z. L. Wang, *ACS Nano* **2014**, *8*, 6031.
[21] L. Lin, Y. N. Xie, S. M. Niu, S. H. Wang, P.-K. Yang, Z. L. Wang, *ACS Nano* **2015**, *9*, 922.

FULL PAPER

[22] M.-H. Yeh, H. Guo, L. Lin, Z. Wen, Z. Li, C. Hu, Z. L. Wang, *Adv. Funct. Mater.* **2015**, *26*, 1054.

[23] Y. Zi, S. Niu, J. Wang, Z. Wen, W. Tang, Z. L. Wang, *Nat. Commun.* **2015**, *6*, 8376.

[24] T. Jiang, X. Chen, C. B. Han, W. Tang, Z. L. Wang, *Adv. Funct. Mater.* **2015**, *25*, 2928.

[25] S. M. Niu, Y. Liu, X. Chen, S. H. Wang, Y. S. Zhou, L. Lin, Y. N. Xie, Z. L. Wang, *Nano Energy* **2015**, *12*, 760.

[26] S. M. Niu, Y. Liu, S. H. Wang, L. Lin, Y. S. Zhou, Y. F. Hu, Z. L. Wang, *Adv. Mater.* **2013**, *25*, 6184.

[27] T. Jiang, X. Chen, K. Yang, C. B. Han, W. Tang, Z. L. Wang, *Nano Res.* **2016**, DOI: 10.1007/s12274-016-0997-x.

[28] S. M. Niu, Z. L. Wang, *Nano Energy* **2015**, *14*, 161.

[29] T. Jiang, L. M. Zhang, X. Chen, C. B. Han, W. Tang, C. Zhang, L. Xu, Z. L. Wang, *ACS Nano* **2015**, *9*, 12562.

[30] S. M. Niu, Y. Liu, S. H. Wang, L. Lin, Y. S. Zhou, Y. F. Hu, Z. L. Wang, *Adv. Funct. Mater.* **2014**, *24*, 3332.

[31] S. M. Niu, S. H. Wang, Y. Liu, Y. S. Zhou, L. Lin, Y. F. Hu, K. C. Pradel, Z. L. Wang, *Energy Environ. Sci.* **2014**, *7*, 2339.